Turkish Journal of Science & Technology
17(1), 65-77, 2022

Research Paper
https://doi.org/10.55525/tjst.1061699

MUSIC Based Microwave Imaging of Nonlinear Point-Like Scatterers

Cüneyt UTKU[1*]
[1] Informatics and Information Security Research Center, Scientific and Technological Research Council of Turkey, Kocaeli, Turkey
[*1] cuneyt.utku@tubitak.gov.tr

(Geliş/Received: 23/01/2022; Kabul/Accepted: 05/02/2022)

Abstract: Narrowband localization of point-like nonlinear scatterers in a homogeneous background medium is investigated. A theoretical framework is provided based on Multiple Signal Classification (MUSIC) imaging, formerly developed for time-reversal imaging of point-like targets in cluttered environment. Numerical simulations are provided to assist in understanding the relations between various aspects of the imaging method. Numerical evidence shows that for the same signal to noise ratio, higher order harmonics (second and third harmonics) resulting from nonlinear scattering, have better imaging resolutions compared to the fundamental harmonic corresponding to linear scattering.

Key words: Harmonic radar, nonlinear target, microwave imaging, MUSIC.

Lineer Olmayan Noktasalımsı Saçıcıların MUSIC Tabanlı Mikrodalga Görüntülemesi

Öz: Homojen ortamda lineer olmayan noktasalımsı saçıcıların darbant lokalizasyonu incelenmiştir. Noktasalımsı hedeflerin parazit yankılı ortamda zaman evirme (time reversal) görüntülenmesi için daha önce geliştirilmiş olan Multiple Signal Classification (MUSIC) görüntülemesine dayalı teorik çerçeve sunulmuştur. Görüntüleme metodunun muhtelif yönleri arasındaki ilişkilerin anlaşılması için sayısal benzetimler verilmiştir. Sayısal sonuçlar, aynı sinyal-gürültü oranı için lineer olmayan saçılmadan kaynaklanan yüksek mertebeden harmoniklerin (ikinci ve üçüncü harmonikler), lineer saçılmaya tekabul eden temel harmoniğe nisbetle daha iyi görüntüleme çözünürlüğüne sahip olduklarını göstermektedir.

Anahtar kelimeler: Harmonik radar, lineer olmayan hedef, mikrodalga görüntüleme, MUSIC.

1. Introduction

Harmonic radars have received considerable attention in recent years mainly due to their inherent clutter rejecting nature. Harmonic radars using passive transponders/tags have been proposed for diverse applications such as tracking [1,2], monitoring of vital signs [3], search and rescue of people under distress [4,5] and in standoff measurement of temperature [6]. Recent advances on harmonic tag applications can be found in [7]. Another very important application of harmonic radars is the detection of concealed electronics [8,9]. Most of the above applications require localization of these harmonic generating tags or devices. Two imaging based localization strategies of nonlinear targets have been proposed in the past. Both are broadband systems operating in stepped frequency mode. The first system based on synthetic aperture radar (SAR) processing was proposed for two-dimensional localization of stationary nonlinear scatterers [10]. With later improvements the system was modified to locate and also estimate the speed of moving nonlinear scatterers [11]. The second proposed system is based on Robust Capon Beamforming with frequency smoothing and has improved imaging quality compared the former SAR based system for stationary targets [12].

In contrast to the aforementioned imaging methods, this study focuses on narrowband and near field imaging of point-like nonlinear targets/scatterers embedded in a homogeneous background medium. A MUSIC based imaging method, which was originally proposed [13-15] as an alternative to conventional time-reversal imaging, is adopted here. The time reversal matrix can be decomposed into a product of the multistatic response matrix/transfer matrix (corresponding to a set linear targets and an associated transmit/receive array configuration) and its Hermitian [16]. With this decomposition, Lev-Ari and Devaney [13], Devaney [14] and Devaney et al [15] used the MUSIC framework to classify the singular system of the multistatic response matrix into its signal and

* Corresponding author: cuneyt.utku@tubitak.gov.tr. ORCID Number of authors: [1] 0000-0002-0993-5545

noise subspaces and exploited the orthogonality of these subspaces to define a pseudo-spectrum that peaked at the target locations. In this study, the multistatic response matrix, originally defined for linear scatterers, is generalized for nonlinear scatterers to a set of multistatic response matrices and the MUSIC framework is similarly applied to this new set of multistatic response matrices to image point-like nonlinear scatterers.

In the next section, the signal model for EM fields measured by an array of antenna elements is discussed, followed by adaptation of the signal model to MUSIC based imaging. Numerical simulations are presented, investigating important aspects of the MUSIC based imaging. A summary of the findings along with short discussions is provided in the conclusion.

2. The Signal Model and MUSIC Imaging

Consider a collection of M nonlinear point-like scatterers embedded in a homogeneous background medium with relative permittivity ε_{rb}. We are interested in estimating the location of these scatterers by probing the collection with time harmonic EM waves at frequency f (a time dependence of $\exp\{-i\omega t\}$ is assumed where $\omega = 2\pi f$) using a distributed system of N antennas operating both in transmit and receive modes i.e. transmitters and receivers are collocated. In this study, it is assumed that $M \leq N$ and multiple scattering between scatterers is assumed to be negligible so that the results are valid to first order of scattering. Moreover, the problem is treated in two dimensions for simplicity. The two-dimensional treatment is not a restriction, however, and generalization of the following mathematical development to three dimensions is possible with some rigour. The problem geometry is depicted in Figure 1 where the point-like scatterers correspond to infinite length lines aligned with z-axis, having nonlinear scattering characteristics. Similarly, the system of RX/TX antennas is a uniform linear array of line sources aligned with z-axis. The array axis runs parallel to the x-axis and is located in the region $y < 0$. Array length is given by $\mathcal{L} = Nd$ where N is the number of array elements and d is the array inter-element spacing. The region of interest (ROI) is the region subject to imaging and is conservatively selected between $[-\mathcal{L}/2\,, \mathcal{L}/2]$ in the x-direction and between $[0, \mathcal{L}/2]$ in the y-direction. Also shown in the figure is a grid comprising the actual pixels of the image. The grid spacings are Δ_x and Δ_y along the x- and y-axis, respectively. These spacings do not necessarily correspond to the imaging resolution to be discussed later. In two dimensions, the problem can be treated with scalar formalism, so for the geometry considered here, the electric field normal to the xy-plane is sufficient to completely determine the problem. Let the scalar quantity $E(\boldsymbol{x}_r, \boldsymbol{x}_t)$ denote the electric field along z-axis, received by the antenna at $\boldsymbol{x}_r \in \{\boldsymbol{x}_1, \cdots, \boldsymbol{x}_N\}$ when the antenna (line source) at $\boldsymbol{x}_t \in \{\boldsymbol{x}_1, \cdots, \boldsymbol{x}_N\}$ is in transmission. This field can be expressed as the sum of all the harmonics generated by nonlinearity [9, 19] (the DC component is suppressed):

$$E(\boldsymbol{x}_r, \boldsymbol{x}_t, t) = \sum_{n=1}^{\infty} E^{(n)}(\boldsymbol{x}_r, \boldsymbol{x}_t)\, e^{-in\omega t} \tag{1}$$

where

$$E^{(n)}(\boldsymbol{x}_r, \boldsymbol{x}_t) \approx \sum_{m=1}^{M} \alpha_m^{(n)} G(\boldsymbol{x}_r, \boldsymbol{x}_m, n\omega) G^n(\boldsymbol{x}_m, \boldsymbol{x}_t, \omega) b^n \tag{2}$$

is the electric field (z-axis) corresponding to the n'th harmonic scattered by M nonlinear particles, $\alpha_m^{(n)}$ is a nonlinearity coefficient for the m'th particle corresponding to the n'th harmonic, b is the amplitude of the time harmonic signal transmitted by the antenna (line source) and $G(\boldsymbol{x}, \boldsymbol{x}', \omega)$ is the two dimensional Green's function for a line source at $\boldsymbol{x}'$ and observation point at $\boldsymbol{x}$. The Green' function is given by $G(\boldsymbol{x}, \boldsymbol{x}', \omega) = (i/4) H_0^{(1)}\left(|\boldsymbol{x} - \boldsymbol{x}'|\, \omega\sqrt{\varepsilon_{rb}}/c\right)$ where $H_0^{(1)}(\cdot)$ is the Hankel function of the first kind and zero order. In deriving

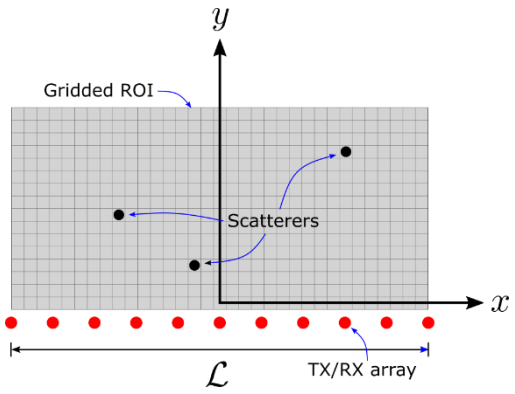

Figure 1. Geometry for imaging of point-like nonlinear scatterers. Red dots indicate the array of length $\mathcal{L}$.

Equation 2, it is reasonably assumed that $Q_m^{2(q+1)} \ll Q_m^{2q}$ and $Q_m^{2(q+1)+1} \ll Q_m^{2q+1}$ for $\forall\, q \in \mathbb{N}$ where $Q_m^n = \left|\alpha_m^{(n)} G^n(\boldsymbol{x}_m, \boldsymbol{x}_t, \omega) b^n\right|$. We restate that the effect of multiple scattering between scatterers is neglected so that Equation 2 is correct to first order of scattering.

When several elements transmit simultaneously, Equation 2 is modified and the expression for the field corresponding to the n'th harmonic then becomes

$$E^{(n)}(\boldsymbol{x}_r, \tilde{\boldsymbol{x}}_t) = \sum_{m=1}^{M} \alpha_m^{(n)} G(\boldsymbol{x}_r, \boldsymbol{x}_m, n\omega) \left(\sum_{j=1}^{N} b_j G\left(\boldsymbol{x}_m, \boldsymbol{x}_{t,j}, \omega\right) \right)^n$$

where the N-tuple $\tilde{\boldsymbol{x}}_t = (\boldsymbol{x}_1, \cdots, \boldsymbol{x}_N)$ indicates that all N array elements are in transmission mode and b_j is the amplitude of the signal transmitted by the j'th transmitting element. One can expand the above expression as

$$E^{(n)}(\boldsymbol{x}_r, \tilde{\boldsymbol{x}}_t) = E_L^{(n)}(\boldsymbol{x}_r, \tilde{\boldsymbol{x}}_t) + \sum_{m=1}^{M} \alpha_m^{(n)} G(\boldsymbol{x}_r, \boldsymbol{x}_m, n\omega) B(\boldsymbol{x}_m, \tilde{\boldsymbol{x}}_t)$$

where

$$E_L^{(n)}(\boldsymbol{x}_r, \tilde{\boldsymbol{x}}_t) = \sum_{m=1}^{M} \alpha_m^{(n)} G(\boldsymbol{x}_r, \boldsymbol{x}_m, n\omega) \sum_{j=1}^{N} G^n\left(\boldsymbol{x}_m, \boldsymbol{x}_{t,j}, \omega\right) b_j^n$$

and $B(\boldsymbol{x}_m, \tilde{\boldsymbol{x}}_t)$ contains all the remaining cross product terms. Changing the order of summation in the last expression and making use of the definition in Equation 2, one has $E_L^{(n)}(\boldsymbol{x}_r, \tilde{\boldsymbol{x}}_t) = \sum_{j=1}^{N} E^{(n)}\left(\boldsymbol{x}_r, \boldsymbol{x}_j\right)$ suggesting that $E_L^{(n)}(\boldsymbol{x}_r, \tilde{\boldsymbol{x}}_t)$ can be obtained as sum of the isolated measurements $E^{(n)}\left(\boldsymbol{x}_r, \boldsymbol{x}_j\right), j = 1, \ldots, N$, i.e. the measurement made when only the array element at $\boldsymbol{x}_j$ is in transmission. Collecting the results of all N receivers in a vector $\boldsymbol{E}_L^{(n)} = \left[E_L^{(n)}(\boldsymbol{x}_1, \tilde{\boldsymbol{x}}_t), \cdots, E_L^{(n)}(\boldsymbol{x}_N, \tilde{\boldsymbol{x}}_t)\right]^T$ where the superscript 'T' denotes the transpose, one has the matrix expression

$$\boldsymbol{E}_L^{(n)} = \boldsymbol{K}^{(n)}\boldsymbol{b}^{(n)} \tag{3}$$

where $\boldsymbol{b}^{(n)} = [b_1^n, \cdots, b_N^n]^T$ and

$$\boldsymbol{K}^{(n)} = \sum_{m=1}^{M} \boldsymbol{K}_m^{(n)} \tag{4}$$

is the multistatic response matrix corresponding to the n'th harmonic, that maps the N dimensional complex space to itself i.e. $\boldsymbol{K}^{(n)}: C^N \to C^N$. Similarly, $\boldsymbol{K}_m^{(n)}$ is the multistatic response matrix for the m'th scatterer, corresponding to the n'th harmonic. The elements of $\boldsymbol{K}_m^{(n)}$ are given as

$$\left[\boldsymbol{K}_m^{(n)}\right]_{ij} = \alpha_m^{(n)} G(\boldsymbol{x}_i, \boldsymbol{x}_m, n\omega) G^n\left(\boldsymbol{x}_m, \boldsymbol{x}_j, \omega\right). \tag{5}$$

Further defining the vector quantities

$$\boldsymbol{g}_{r,m}^{(n)} = [G(\boldsymbol{x}_1, \boldsymbol{x}_m, n\omega), \cdots, G(\boldsymbol{x}_N, \boldsymbol{x}_m, n\omega)]^T \tag{6}$$

and

$$\boldsymbol{g}_{t,m}^{(n)} = [G^n(\boldsymbol{x}_1, \boldsymbol{x}_m, \omega), \cdots, G^n(\boldsymbol{x}_N, \boldsymbol{x}_m, \omega)]^T, \tag{7}$$

the multistatic response matrix can alternatively be expressed as:

$$\boldsymbol{K}_m^{(n)} = \alpha_m^{(n)} \boldsymbol{g}_{r,m}^{(n)} \left[\boldsymbol{g}_{t,m}^{(n)}\right]^T. \tag{8}$$

Note that for the fundamental harmonic i.e. $n = 1$, $\boldsymbol{g}_{r,m}^{(1)} = \boldsymbol{g}_{t,m}^{(1)}$, so that the above expressions readily reduce to those given in literature (e.g. [14]) for collocated transmitters and receivers. For the fundamental harmonic, whenever $\left[\boldsymbol{g}_{r,k}^{(1)}\right]^T \boldsymbol{g}_{t,m}^{(1)*} = \left[\boldsymbol{g}_{t,k}^{(1)}\right]^T \boldsymbol{g}_{t,m}^{(1)*} = \delta_{k,m}$ where $\delta_{k,m}$ is the Kronecker delta, the scatterers k and m are said to be resolved [14]. This notion may be generalized to nonlinear scatterers such that nonlinear scatterers k and m are said to be resolved at the n'th harmonic whenever $\left[\boldsymbol{g}_{r,k}^{(n)}\right]^T \boldsymbol{g}_{t,m}^{(n)*} = \delta_{k,m}$. Hence, scatterers that are not resolved at the fundamental harmonic may be resolved at a higher order harmonic. If all scatterers are resolvable at the n'th harmonic then the explicit expression of Equation 4, given as (using Equation 8)

$$\boldsymbol{K}^{(n)} = \sum_{m=1}^{M} \alpha_m^{(n)} \boldsymbol{g}_{r,m}^{(n)} \left[\boldsymbol{g}_{t,m}^{(n)}\right]^T, \tag{9}$$

becomes the singular value decomposition (SVD) of $\boldsymbol{K}^{(n)}$ where $\alpha_m^{(n)}$ corresponds to the singular value with left and right singular vectors $\boldsymbol{g}_{r,m}^{(n)}$ and $\boldsymbol{g}_{t,m}^{(n)*}$, respectively. For particles that are non-resolvable at the n'th harmonic, the multistatic response matrix bears an SVD as $\boldsymbol{K}^{(n)} = \boldsymbol{U}^{(n)}\boldsymbol{\Lambda}^{(n)}\left[\boldsymbol{V}^{(n)}\right]^H$ where the superscript 'H' denotes the Hermitian, $\boldsymbol{\Lambda}^{(n)}$ is an $N \times N$ diagonal matrix of singular values $\sigma_1^{(n)} \geq \cdots \geq \sigma_M^{(n)} > \sigma_{M+1}^{(n)} = \cdots = \sigma_N^{(n)} = 0$ and $\boldsymbol{U}^{(n)} = \left[\boldsymbol{u}_1^{(n)}, \ldots, \boldsymbol{u}_N^{(n)}\right]$ and $\boldsymbol{V}^{(n)} = \left[\boldsymbol{v}_1^{(n)}, \ldots, \boldsymbol{v}_N^{(n)}\right]$ are $N \times N$ orthonormal matrices with columns corresponding to the left and right singular vectors, respectively. In this case however, the left and right singular vectors do not

coincide with the vectors $\boldsymbol{g}_{r,m}^{(n)}$ and $\boldsymbol{g}_{t,m}^{(n)*}$, respectively. Yet, one observes that the matrix $\boldsymbol{g}_{r,m}^{(n)}\left[\boldsymbol{g}_{t,m}^{(n)}\right]^T$ of rank 1, maps the one dimensional subspace (a line) spanned by the vector $\boldsymbol{g}_{t,m}^{(n)*}$ into the one dimensional subspace spanned by the vector $\boldsymbol{g}_{r,m}^{(n)}$ so that $\boldsymbol{K}^{(n)}$ is a one to one mapping from $span\left\{\boldsymbol{g}_{t,1}^{(n)},\dots,\boldsymbol{g}_{t,M}^{(n)}\right\}$ to $span\left\{\boldsymbol{g}_{r,1}^{(n)},\dots,\boldsymbol{g}_{r,M}^{(n)}\right\}$. As a result, one has $span\left\{\boldsymbol{g}_{t,1}^{(n)},\dots,\boldsymbol{g}_{t,M}^{(n)}\right\}\subseteq span\left\{\boldsymbol{v}_1^{(n)},\dots,\boldsymbol{v}_M^{(n)}\right\}$ and $span\left\{\boldsymbol{g}_{r,1}^{(n)},\dots,\boldsymbol{g}_{r,M}^{(n)}\right\}\subseteq span\left\{\boldsymbol{u}_1^{(n)},\dots,\boldsymbol{u}_M^{(n)}\right\}$. Since $\boldsymbol{V}^{(n)}$ is an orthogonal matrix, it follows that $\left[\boldsymbol{v}_i^{(n)}\right]^H\boldsymbol{g}_{t,m}^{(n)*}=0$ for $i=M+1,\dots,N$ i.e. the null space of $\boldsymbol{K}^{(n)}$, determined as $span\left\{\boldsymbol{v}_{M+1}^{(n)},\dots,\boldsymbol{v}_N^{(n)}\right\}$, is orthogonal to $span\left\{\boldsymbol{g}_{t,1}^{(n)},\dots,\boldsymbol{g}_{t,M}^{(n)}\right\}$. Following [14], the location of the nonlinear scatterers may now be determined by employing the MUSIC algorithm, implemented by defining the steering vector $\boldsymbol{g}_t^{(n)}(\boldsymbol{x})=[G^n(\boldsymbol{x}_1,\boldsymbol{x},\omega),\cdots,G^n(\boldsymbol{x}_N,\boldsymbol{x},\omega)]^T$ and the pseudo-spectrum for the n'th harmonic

$$p^{(n)}(\boldsymbol{x})=\frac{1}{\sum_{i=M+1}^{N}\left|\left[\boldsymbol{v}_i^{(n)}\right]^H\boldsymbol{g}_t^{(n)*}(\boldsymbol{x})\right|}. \tag{10}$$

On a finite grid, the pseudo-spectrum is a false image of the scattering potential over the grid (ROI) and its value will peak at a pixel containing the scatterer since $p^{(n)}(\boldsymbol{x}=\boldsymbol{x}_m)=\infty$ for $m=1,\dots,M$. Note that alternative pseudo spectra can also be defined using the left singular vectors as in [15,17,18] or using both left and right singular vectors but these alternatives are not pursued in this study for conciseness.

2.1 Effect of Noise in Measurements

The effect of measurement noise has been neglected in the preceeding discussion. In reality, the multistatic response matrix is constructed from noisy measurements of $\boldsymbol{E}_L^{(n)}$. The measurement equation is of the form $\boldsymbol{E}_L^{(n)}=\boldsymbol{K}^{(n)}\boldsymbol{b}^{(n)}+\boldsymbol{n}$ where $\boldsymbol{n}$ is a measurement noise vector of length N added to the relation in Equation 3. With noise present, the noisy multistatic response matrix $\widetilde{\boldsymbol{K}}^{(n)}$ is in general of full rank implying that $\tilde{\sigma}_i>0,\forall i=1,\dots,N$. The addition of noise will perturb the singular system $(\boldsymbol{u}_i,\sigma_i,\boldsymbol{v}_i)$, $i=1,\dots,N$, of $\boldsymbol{K}^{(n)}$ resulting in the new singular system $(\widetilde{\boldsymbol{u}}_i,\tilde{\sigma}_i,\widetilde{\boldsymbol{v}}_i)$ for $\widetilde{\boldsymbol{K}}^{(n)}$. In the nomenclature of MUSIC, $\mathcal{S}=span\{\widetilde{\boldsymbol{v}}_1,\dots,\widetilde{\boldsymbol{v}}_M\}$ is known as the *signal* subspace and $\mathcal{N}=span\{\widetilde{\boldsymbol{v}}_{M+1},\dots,\widetilde{\boldsymbol{v}}_N\}$ is known as the *noise* subspace. The signal and noise subspaces are again orthogonal to each other but because the singular system $(\widetilde{\boldsymbol{u}}_i,\tilde{\sigma}_i,\widetilde{\boldsymbol{v}}_i)$ is perturbed from the original noise-free $(\boldsymbol{u}_i,\sigma_i,\boldsymbol{v}_i)$ system, the vectors $\boldsymbol{g}_{t,m}^{(n)}$, $m=1,\dots,M$, will have non-zero projections onto both subspaces. Moreover, because M is not known a priori, the signal and noise subspaces must be identified by some appropriate means. Such a distinction between signal and noise subspaces may be not even be possible if the signal to noise ratio (SNR) is close to or less than unity. A common method for signal and noise subspace identification is to use a threshold $\epsilon_{th}^{(n)}$ such that singular vectors corresponding $\tilde{\sigma}_i^{(n)}\geq\epsilon_{th}^{(n)}$ are designated the signal subspace and singular vectors corresponding $\tilde{\sigma}_i^{(n)}<\epsilon_{th}^{(n)}$ are designated the noise subspace [14]. Formally, one has $\mathcal{S}=\left\{\widetilde{\boldsymbol{v}}_i\mid\tilde{\sigma}_i^{(n)}\geq\epsilon_{th}^{(n)}\right\}$ and $\mathcal{N}=\left\{\widetilde{\boldsymbol{v}}_i\mid\tilde{\sigma}_i^{(n)}<\epsilon_{th}^{(n)}\right\}$. With the proviso that the signal and noise subspaces can be identified, a false image of the scattering potential is constructed using the pseudo-spectrum

$$\tilde{p}^{(n)}(\boldsymbol{x})=\frac{1}{\sum_{\widetilde{\boldsymbol{v}}_i^{(n)}\in\mathcal{N}}\left|\left[\widetilde{\boldsymbol{v}}_i^{(n)}\right]^T\boldsymbol{g}_t^{(n)*}(\boldsymbol{x})\right|}. \tag{11}$$

This pseudo-spectrum will peak at $\boldsymbol{x} = \boldsymbol{x}_m, k = 1, \cdots, M$, yielding the locations of isolated point-like nonlinear scatterers. In the following, the quantity defined as $I^{(n)}(i,j) = 10\log\left(\tilde{p}^{(n)}(x_i, y_j)\right)$ will be designated as the image corresponding to the n'th harmonic.

3. Numerical Simulations

In this section, the pseudo-spectrum defined in Equation 11, is applied to several imaging scenarios using numerical simulations. Simulation geometry is depicted in Figure 1 with free space as the background medium ($\varepsilon_{rb} = 1$). Throughout, the fundamental frequency is $f = 2.4$ GHz and only the first three harmonics, namely $f, 2f$ and $3f$, are considered. A grid spacing of $\Delta_x = \Delta_y = \lambda_3/10$ and an array inter-element distance of $d = \lambda_3/2$ is assumed where $\lambda_n = c/nf$ is the wavelength of the n'th harmonic. This choice of d is made to prevent spatial aliasing for all three harmonics. The array is also located at $y = -d$. Furthermore, additive Gaussian noise is assumed for the simulations and SNR is defined with respect to the mean magnitude of the multistatic matrix elements. For simplicity, the signal and noise subspaces will be determined directly by M.

In the first set of simulations, the number of scatterers $M = 6$ and the number of array elements $N = 21$. The scattering potentials for the scatterers are selected conveniently as $\alpha_m^{(n)} = 1$ for $m = 1, \ldots, M$ and $n = 1,2,3$. In Figure 2, the image $I^{(1)}$, for the first (fundamental) harmonic is shown on the left for $SNR = 10$ dB (Figure 2a) and on the right for $SNR = 20$ dB (Figure2b). These images are constructed assuming that M is known. The black crosses in the images indicate the actual locations of the scatterers. It is seen in Figure 2a that long bright streaks exist for 10 dB SNR. Although the streaks contain the scatterers, it is not possible to determine the actual number and the locations of the scatterers. For the higher SNR of 20 dB, it is observed in Figure 2b that the bright streaks have contracted considerably. The bright regions in the improved image facilitates identification of at least five scatterers. The size of the bright regions also grows with distance from the array indicating increase in localization uncertainty further away from the array.

The image $I^{(2)}$, corresponding to the second harmonic, is shown in Figure 3a for $SNR = 10$ dB and in Figure 3b for $SNR = 20$ dB. In both figures, all six scatterers can be distinguished from $I^{(2)}$. Compared to Figure 2a of $I^{(1)}$ with 10 dB SNR, $I^{(2)}$ with an SNR of 10 dB appears to have smaller uncertainty in locations of the three scatterers the closest to the array. However, compared to Figure 2, the background intensity has increased toward

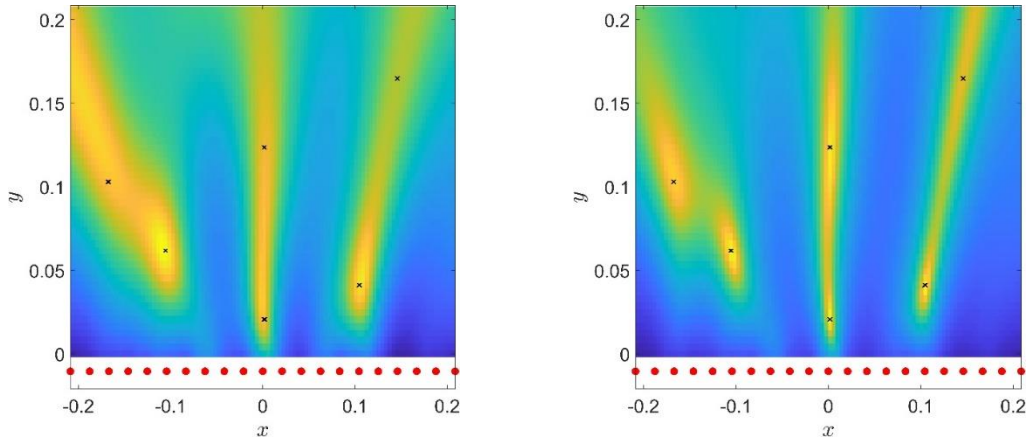

Figure 2. First (fundamental) harmonic image (MUSIC pseudo-spectrum) of $M = 6$ nonlinear point-like scatterers with $N = 21$ array elements for (a) $SNR = 10$ dB and (b) $SNR = 20$ dB.

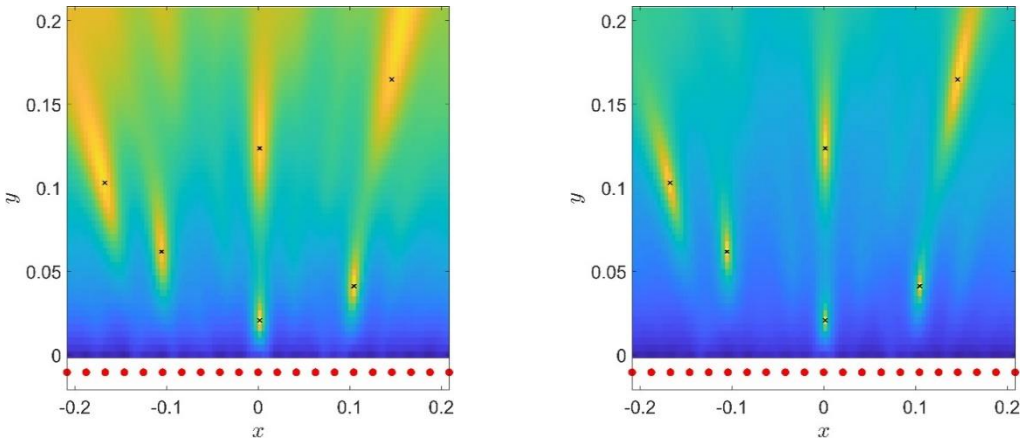

(a) (b)

Figure 3. Second harmonic image of $M = 6$ nonlinear point-like scatterers with $N = 21$ array elements for (a) $SNR = 10$ dB and (b) $SNR = 20$ dB.

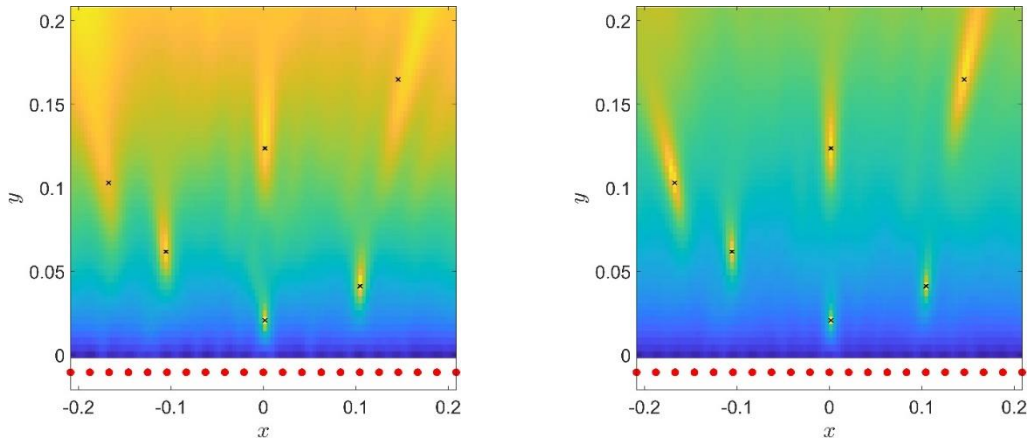

(a) (b)

Figure 4. Third harmonic image of $M = 6$ nonlinear point-like scatterers with $N = 21$ array elements for (a) $SNR = 10$ dB and (b) $SNR = 20$ dB.

the top (far) end of the image, causing a decrease in contrast specially to the left of the image. The image $I^{(2)}$ in Figure 3b corresponding the 20 dB SNR shows further improvement such that uncertainty has decreased considerably for all scatterer locations. These two figures suggest that the second harmonic is more robust to measurement noise compared to the fundamental harmonic.

The final image $I^{(3)}$, corresponding to the third harmonic is shown in Figure 4a for $SNR = 10$ dB and in Figure 4b for $SNR = 20$ dB. The most striking feature in the image of Figure 4a is the high background intensity of the image and although the presence of the bright streaks near the top end of the image suggest the presence of at least the three existing scatterers, it is not possible the determine the actual number of scatterers. Nevertheless, the closest three scatterers to the array are clearly resolved with little uncertainty. This is an improvement compared

to $I^{(1)}$ for the same SNR. For $SNR = 20$ dB, it appears in Figure 4b that the third harmonic provides no further improvement over $I^{(2)}$ shown in Figure 3b.

The preceeding analysis instigates further investigation into the relation between resolution, noise and harmonic order. Here, resolution is defined as the minimum distance between two scatterers such that the scatterers are distinguishable. Resolution is related to the spread of the peaks (poles) of the pseudo-spectrum $\tilde{p}^{(n)}(\boldsymbol{x})$ which is regulated by the level of noise (SNR), the number of array elements N, and the wavelength of the harmonic. As seen from the above figures (Figure 2 – Figure 4), resolution is also expected to be a function of distance from the array degrading with increasing distance. Furthermore, it is also evident from the orientations of the streaks in the figures (extending away from the array and almost normal to the array near the center) that resolutions along the x- and y-axis are very different. To substantiate some of these arguments, consider the two scenarios with $N = 21$, where in the first scenario two scatterers are separated along the x-axis to investigate resolution along array axis and in the second scenario two scatterers are separated along the y-axis to investigate resolution along the normal to array axis. Specifically, in the first scenario the two scatterer locations coordinates are $(-\delta_s/2\,, h)$ and $(\delta_s/2, h)$, respectively, where $\delta_s = \lambda_1/10$ and $h = \lambda_1/4$. In the second scenario, the two scatterer location coordinates are $(0, h - \delta_s/2)$ and $(0, h + \delta_s/2)$, respectively. For the first scenario, the normalized (relative to its maximum value) sample pseudo-spectrums $\tilde{p}^{(n)}(\boldsymbol{x})$ for $n = 1,2,3$, are plotted in Figure 5a along the line $y = h$. Similarly, for the second scenario, the normalized sample $\tilde{p}^{(n)}(\boldsymbol{x})$ for $n = 1,2,3$, are plotted in Figure 5b along the line $x = 0$. In both figures, an SNR of 20 dB is assumed for all harmonics. In Figure 5a, $\tilde{p}^{(1)}$ for the fundamental harmonic (red line) cannot resolve the two scatterers while both $\tilde{p}^{(2)}$ for the second harmonic (green line) and $\tilde{p}^{(3)}$ for the third harmonic (blue line) can distinguish the two scatterers very close to their correct locations. Note also that $\tilde{p}^{(3)}$ is sharper than $\tilde{p}^{(2)}$ suggesting that higher harmonics have better resolution for $h = \lambda_1/4$. In the second scenario on the other hand, it is observed from Figure 5b that the pseudo-spectrums for the first two harmonics cannot resolve the scatterers while the third harmonic can resolve the two scatterers near their correct locations. Also, the curves in the latter figure are not symmetric about the point $y/\lambda_1 = 0.25$, because the left end of the plots is closer to the array. Near the right end of the plots (further to the array), $\tilde{p}^{(2)}$ and $\tilde{p}^{(3)}$ are higher than $\tilde{p}^{(1)}$ likely due to the relative decrease in the magnitude of the steering vector $\boldsymbol{g}_t^{(n)}(\boldsymbol{x})$, appearing denominator in Equation 11, with increasing distance away from the array. This phenomenon was observed in Figure 3b and Figure 4b as the high background intensity in the images. The pseudo-spectrums in the second scenario are broader than those of in first scenario, causing loss of resolution. This concludes that resolution is better along array axis.

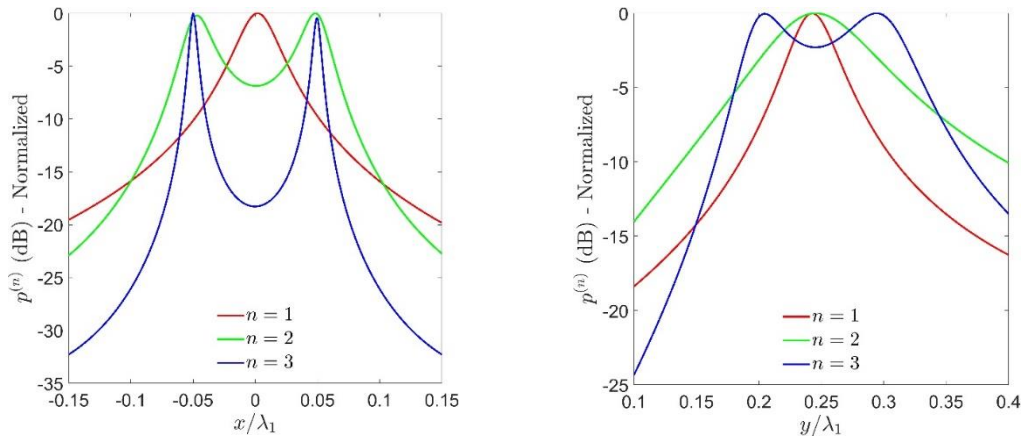

(a) (b)

Figure 5. Normalized pseudo-spectrum for two nonlinear point-like scatterers along x-axis (a) and along y-axis (b) for $SNR = 20$ dB and with $N = 21$ array elements.

To further observe the effect of noise on resolution, the above two scenarios are repeated with an SNR of 10 dB. The pseudo-spectrums for the first scenario are plotted in Figure 6a and those for the second scenario are plotted in Figure 6b. In contrast to Figure 5a, the green curve corresponding to $\tilde{p}^{(2)}$ in Figure 6a can no longer resolve the two scatterers along the x-axis. The blue curve corresponding to $\tilde{p}^{(3)}$ can still resolve the two scatterers near their correct locations but the spread of peaks is now broader due to the adverse effect of noise. For the second scenario, the plots in Figure 6b show that none of the harmonics can now resolve the two scatterers. The higher values for the second and third harmonics near the right end of the plots are again indicative of the higher intensities near the top end of the images in Figure 3a and Figure 4a. The conclusion is that noise causes broadening of the peaks in the pseudo-spectrums. As can be observed in the behavior of $\tilde{p}^{(3)}$ in Figure 5b and Figure 6b, this broadening causes the peaks corresponding to two close scatterers to progressively overlap as SNR decreases. Eventually, these peaks will merge into a single peak resulting in a decline in resolution.

For an array with fixed inter-element distance d, resolution for a given SNR can be improved by increasing the number of array elements N, as a result of sharpening of the peaks with increased array length. This is demonstrated using the normalized $\tilde{p}^{(3)}$ (third harmonic) with $SNR = 10$ dB in Figure 7a for the first scenario and in Figure 7b for the second scenario. In both figures, solid curves correspond to the case with $N = 21$ elements and dashed curves correspond to the case with $N = 101$ elements. In Figure 7a, comparison of the two curves clearly shows that the array with $N = 101$ elements produces a much sharper pseudo-spectrum at the scatterer locations (poles) than the pseudo-spectrum with $N = 21$ elements. Similarly, it is seen in Figure 7b that while the array with $N = 21$ elements is unable to resolve the two scatterers, the array with $= 101$ elements can resolve the scatterers. The conclusion is that longer arrays with more elements can result in better resolution.

The effects of the SNR and the number of elements on resolution are summarized in Figure 8 for the first scenario and in Figure 9 for the second scenario. Each curve in the figures corresponds to a single harmonic and provides a relation between the SNR and the number of array elements N, required to resolve the two scatterers with roughly 50% probability. The curves are generated by Monte-Carlo (MC) simulations with a total of $N_{MC} = 1000$ realizations for each harmonic. In each realization of a MC simulation corresponding to the n'th harmonic,

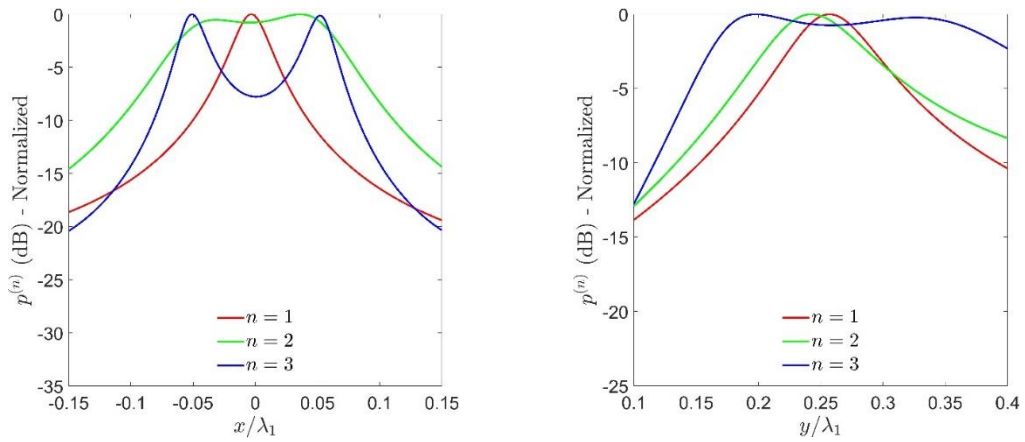

(a) (b)

Figure 6. Normalized pseudo-spectrum for two nonlinear point-like scatterers along x-axis (a) and along y-axis (b) for $SNR = 10$ dB and with $N = 21$ array elements.

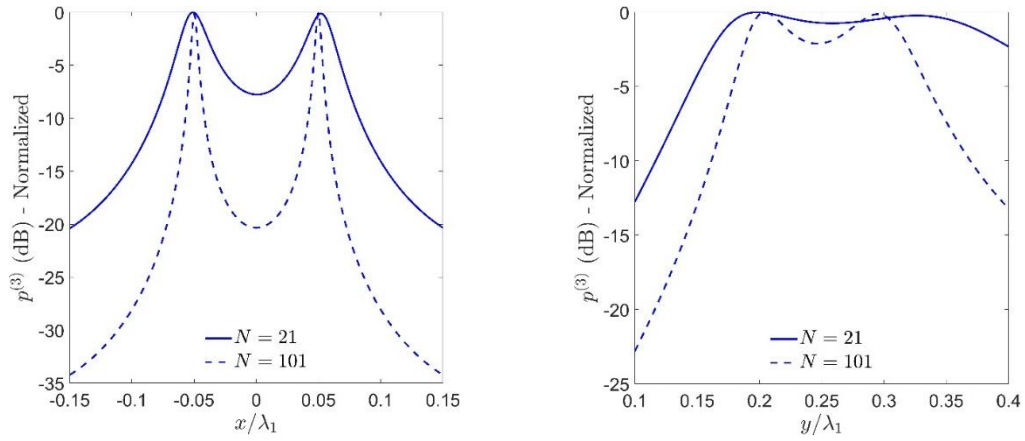

(a) (b)

Figure 7. Normalized pseudo-spectrum (3rd harmonic) for two nonlinear point-like scatterers along x-axis (a) and along y-axis (b) for $SNR = 10$ dB with $N = 21$ (solid line) and $N = 101$ (dashed line) array elements.

a noisy sample of the multistatic response matrice $\widetilde{\boldsymbol{K}}^{(n)}$, is generated. The pseudo-spectrum $\tilde{p}_k^{(n)}$, for the k'th sample ($k = 1, \dots, N_{MC}$) is then computed and the number of peaks $N_{peak,k}^{(n)}$, for the sample is estimated from $\tilde{p}_k^{(n)}$. The expected number of scatterers is obtained by averaging $N_{peak,k}^{(n)}$ over all samples as $\widehat{N}_{peak}^{(n)} = (1/N_{MC}) \sum_{k=1}^{N_{MC}} N_{peak,k}^{(n)}$. Note that $1 \leq \widehat{N}_{peak}^{(n)} \leq 2$ and when $\widehat{N}_{peak}^{(n)} \approx 1$, the two scatterers are not resolved in majority of the samples. In contrast, when $\widehat{N}_p^{(n)} \approx 2$, the two scatterers are resolved in majority of the samples. The curves in the figures correspond to $\widehat{N}_{peak}^{(n)} = 1.5$, which indicates that the two targets are resolved in half of the samples. Hence, further to the right of the curve for the n'th harmonic, it is very likely that the two scatterers

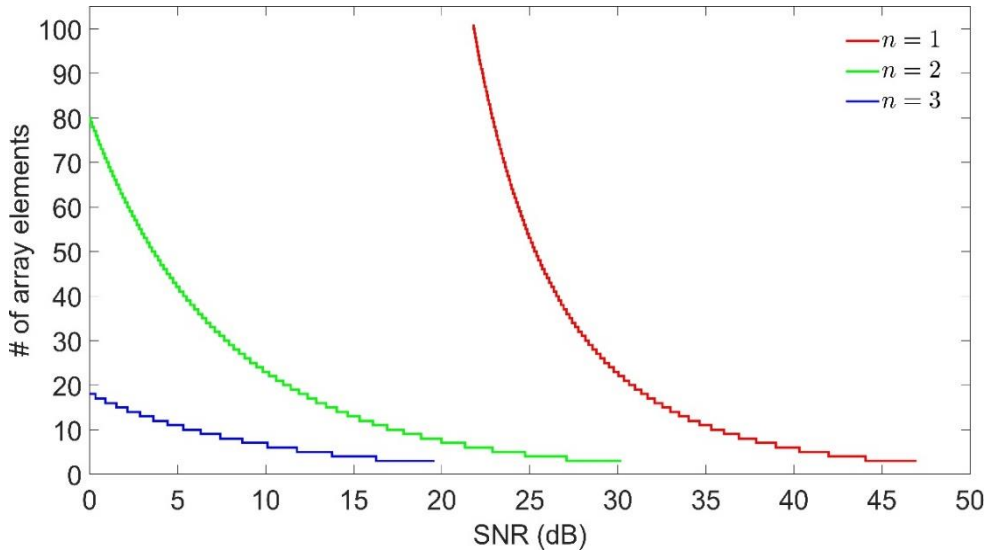

Figure 8. Number of array elements required to resolve two scatterers (with 50% probability) displaced by $\lambda_1/10$ along x-axis vs SNR.

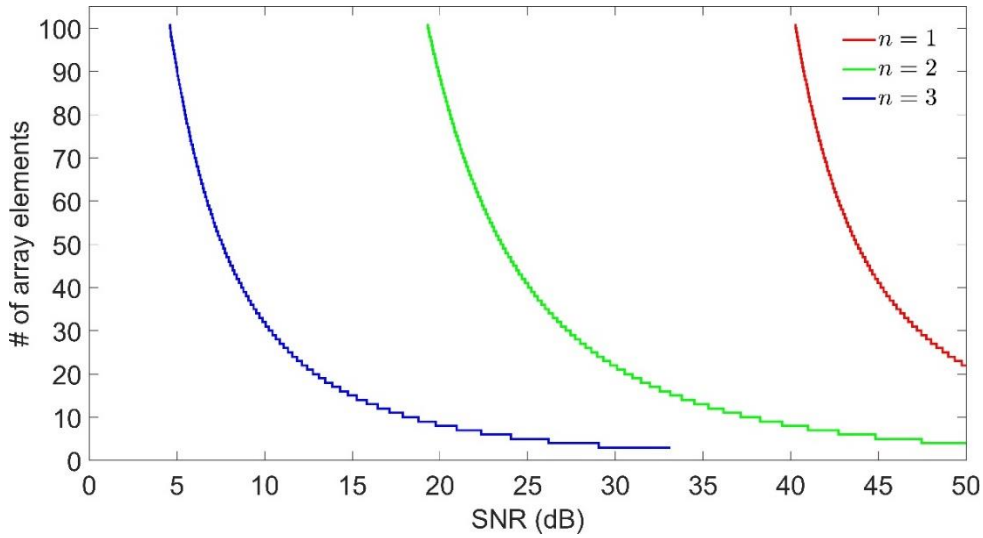

Figure 9. Number of array elements required to resolve two scatterers (with 50% probability) displaced by $\lambda_1/10$ along y-axis vs SNR.

are resolved and further to the left of the curve, it is very unlikely that the two scatterers are resolved by the n'th harmonic.

In both figures, it is observed that irrespective of the harmonic order, more array elements are required to resolve the two scatterers for lower SNR. However, the improvement from additional elements decreases with increasing N as observed by the steep increase in the curves with decreasing SNR. Moreover, curves corresponding to higher order harmonics are shifted further to the left indicating that higher order harmonics require fewer array elements to resolve the scatterers for the same SNR. Finally, comparison of Figure 8 and Figure 9 shows that for each harmonic, fewer number of array elements are required to resolve the two scatterers along the array axis. In fact, it is seen in Figure 9 that below about 5 dB SNR, further increase in N has no effect on the resolution of the third harmonic along the y-axis whereas $N < 20$ is sufficient for the third harmonic to resolve the two scatterers along the x-axis even with SNRs as low as 0 dB. These observations indicate that the resolution along the array axis is superior to that along the array normal.

4. Conclusions

A MUSIC based imaging, previously proposed for improving time-reversal imaging of point-like linear scatterers, is adopted here for imaging of point-like nonlinear scatterers. Unlike previous broadband approaches to localization of nonlinear scatterers, MUSIC based imaging offers a narrowband approach and is better suited for near-field applications. The proposed imaging approach is formulated and simulated in two dimensions for a homogeneous medium. The effect of multiple scattering is neglected which is a reasonable assumption when the point-like scatterers are sufficiently separated. The effect is likely to be stronger in the simulations performed for resolution analysis as the particles were in close proximity of one another. Nevertheless, the results are correct to first order of scattering which accounts for the major effect.

Numerical results show that higher order harmonics can better identify the presence of scatterers and estimate their locations. Higher order harmonics are also more robust to noise near the array of sensors. This is important since the returned signals from the scatterers may be weaker for higher order harmonics. Resolution degrades with distance from the array and also with decrease in SNR. On the other hand, resolution improves with harmonic

order (demonstrated for the first three harmonics) and is also superior along the array axis. The number of array elements plays an important role in resolving of the scatterers so that an array with few elements requires a large SNR to resolve close scatterers whereas an array with many elements can resolve close scatterers with smaller SNR. However, increasing array elements has the cost of dealing with larger multistatic response matrices requiring more field measurements (increasing as N^2). Beyond some trade-off value, increasing the number of elements has a decreasing benefit not justifying the further increase in element number.

The narrowband nature of the of the proposed imaging method is an apparent advantage over the broadband frequency sweeping systems used in [10-12]. But this advantage comes with the cost of increased system complexity due to use all array elements in both transmit and receive modes as opposed to the single transmitting element present in the previous studies. In spite of this drawback, the findings are promising for narrowband, near field imaging of nonlinear scatterers. The current study will be extended to three-dimensional layered media in the future along with experimental work to validate the results. An analysis along the lines of the work done by Ciuonzo et al. [18] for the proposed imaging method is also essential to better gauge its noise performance.

References

[1] Colpitts B.G., Boiteau G., "Harmonic radar transceiver design: Miniature tags for insect tracking," IEEE Antennas and Propagat., vol. 52, no. 11, pp. 2825-2832, 2004.

[2] Jau P.H., Tsai Z.M., Kuo N.C., Kao J.C., Lin K.Y., Chang F.R., Yang E.C., Wang H., "Signal processing for harmonic pulse radar based on spread spectrum technology," IET Radar Sonar Navig., vol. 8, no. 3, pp. 242–250, 2014.

[3] Singh A., Lubecke V.M., "Respiratory monitoring and clutter rejection using a CW Doppler radar with passive RF tags," IEEE Sensors Journal, vol. 12, no. 3, pp. 558-565, 2012.

[4] Granhed M., Forssen K.G., "Sensor-activated transponder," US Patent 20130194100A1, 1 August 2013.

[5] Harzheim T., Muhmel M., Heuermann H., "A SFCW harmonic radar system for maritime search and rescue using passive and active tags,". International Journal of Microwave and Wireless Technologies, vol. 13, pp. 691–707, 2021.

[6] Kubina B., Romeu J., Mandel C., Schussler M., Jakoby R., "Quasi-chipless wireless temperature sensor based on harmonic radar," Electronic Letters, vol. 50, no. 2, pp. 86-88, 2014.

[7] Mondal S., Kumar D., Chahal P., "Recent advances and applications of passive harmonic RFID systems: A review," Micromachines, vol. 12, no. 420, pp. 1-22, 2021.

[8] Lehtola G.E., "RF receiver sensing by harmonic generation," US Patent 7864107B1, 4 January 2011.

[9] Mazzaro G.J., Martone A.F., McNamara D.M., "Detection of RF electronics by multitone harmonic radar" IEEE Trans. On Aerospace and Electronic Sys., vol. 50, no., pp. 477-490, 2014.

[10] Gallagher K.A., "Harmonic Radar: Theory and Applications to Nonlinear Target Detection, Tracking, Imaging and Classification," Ph.D. Dissertation, The Pennsylvania State University, University Park, PA, USA, December 2015.

[11] Gallagher K.A., Narayanan R.M., Mazzaro G.J., Martone A.F., Sherbondy K.D., "Static and moving target imaging using harmonic radar," Electronics, vol. 6, no. 30, pp. 1-20, 2017.

[12] Bischeltsrieder F., Schreiber E., Peichl M., Heinzel A., Jirousek M., "High resolution harmonic radar imaging for safety and security applications," Proceedings of SPIE Conference on Radar Sensor Technology XXIII, vol. 11003, pp. 1-18, Baltimore, MD, May 2019.

[13] Lev-Ari H., Devaney A.J., "The time reversal techniques re-interpreted: Subspace-based signal processing for multistatic target location," Proc. IEEE Sensor Array and Multichannel Signal Processing Workshop, pp. 509-513, Cambridge, MA, March 2000.

[14] Devaney A.J., "Time reversal imaging of obscured targets from multistatic data," IEEE Trans. Antennas Propag., vol. 53, no. 5, pp. 1600-1610, 2005.

[15] Devaney A.J., Marengo E.A., Gruber F.K., "Time-reversal-based imaging and inverse scattering of multiple scattering points," J. Acoust. Soc. Am., vol. 118, no. 5, pp. 3129-3138, 2005.

[16] Prada C., Manneville S., Spoliansky D., Fink M., "Decomposition of the time reversal operator: Detection and selective focusing on two scatterers," J. Acoust. Soc. Am., vol. 99, no. 4, pt. 1, pp. 2067-2076, 1996.

[17] Marengo E.A., Gruber F.K., "Subspace-based localization and inverse scattering of multiply scattering point targets," EURASIP Journal on Advances in Signal Processing, vol. 2007, article ID 17342, 2007, DOI: 10.1155/2007/17342.

[18] Cuionzo D., Romano G., Solimene R., "Performance analysis of time-reversal MUSIC," IEEE Trans. Signal Process., vol. 63, no. 10, pp. 2650-2662, 2015.

[19] Gallagher K.A., Mazzaro G.J., Martone A.F., Sherbondy K.D., Narayanan R.M., "Derivation and validation of the nonlinear radar range equation," Proceedings of SPIE Conference on Radar Sensor Technology Radar Sensor Technology XX, vol. 9829, Baltimore, MD, April 2016.